Molecular Therapy
Oncology
Original Article

Ruxolitinib and oHSV combination therapy increases CD4 T cell activity and germinal center B cell populations in murine sarcoma

Ravi Dhital,[1,5] Yeaseul Kim,[1,5] Doyeon Kim,[1] Ilse Hernandez-Aguirre,[1,2] Jack Hedberg,[1,2] Alexia Martin,[1,2] and Kevin A. Cassady[1,3,4]

[1]Center for Childhood Cancer Research, Abigail Wexner Research Institute at Nationwide Children's Hospital, Columbus, OH, USA; [2]Department of Biomedical Informatics, The Ohio State University College of Medicine, Columbus, OH, USA; [3]Department of Pediatrics, The Ohio State University College of Medicine, Columbus, OH, USA; [4]Department of Pediatrics, Division of Pediatric Infectious Diseases, Nationwide Children's Hospital, Columbus, OH, USA

Malignant peripheral nerve sheath tumors (MPNSTs) are a highly aggressive neoplasm of the peripheral nervous system and are resistant to most conventional cancer therapies. We previously showed that pretreatment with ruxolitinib (RUX) enhanced the efficacy of oncolytic herpes simplex virus (oHSV) virotherapy in this murine sarcoma model. A low abundance of tumor-infiltrating leukocytes and limitations in conventional flow cytometry restrict analyses to a narrow subset of immune cells, potentially introducing a confirmation bias. To address these limitations, we developed a 46-color spectral flow cytometry panel for the detailed analysis of immune cell dynamics following repeated oHSV dosing. Beyond the cytotoxic T lymphocyte (CTL) and regulatory T cell (Treg) changes reported in our earlier studies, RUX+oHSV treatment modulates myeloid and other lymphoid compartments, including germinal center B cell populations with enhanced activation. RUX+oHSV therapy also increased cytokine-expressing CD4(+) populations, predominantly granzyme B(+) cytotoxic-like, interferon (IFN)-γ(+) T helper type 1 (Th1)-like, and interleukin (IL)-21(+) T follicular helper (Tfh)-like phenotypes, within the tumor infiltrates, suggestive of potential tertiary lymphoid structure development in the treated tumors. Here, we illustrate the utility of a high-dimensional spectral flow cytometry panel that permits simultaneous evaluation of intratumoral CD4/CD8 T cell, Treg, γδ-T cell, natural killer T (NKT) cell, B cell, NK cell, monocyte, macrophage, granulocyte, myeloid-derived suppressor cell (MDSC), and dendritic cell functional changes from RUX+oHSV-treated MPNSTs.

INTRODUCTION

Malignant peripheral nerve sheath tumors (MPNSTs) are a highly aggressive neoplasm of the peripheral nervous system, affecting both children and adults. They constitute approximately 10% of all soft-tissue sarcomas, with an annual incidence of 1.46 per million person years and a prevalence of 8%–13% in patients with neurofibromatosis type 1 (NF1).[1,2] These tumors are associated with poor prognosis and stand as the primary cause of mortality in patients with NF1. The 5-year survival rate ranges from 20% to 54%, dropping even further in cases that are unresectable or metastatic.[3] Surgery is the primary treatment for MPNSTs, but most cases are diagnosed at advanced stages, limiting the efficacy of surgical resection. MPNSTs are resistant to conventional therapeutics, and with the lack of FDA-approved drugs for MPNST treatment, clinical trials have explored experimental therapies, such as checkpoint inhibition, macrophage targeting, and oncolytic viruses (OVs).[3,4] OVs, including oncolytic herpes simplex viruses (oHSVs), are modified viruses that selectively replicate in cancer cells, resulting in both tumor cell lysis (oncolysis) and the initiation of an immune response against the tumor (immunotherapy). Pre-clinical studies have shown that tumor-associated immune cell infiltrates are integral to re-establishing immune surveillance.[5,6]

Monitoring immune cell population changes after virotherapy by flow cytometry is integral to delineating cellular and functional changes associated with the treatment response. Comprehensive assessment of immune effector infiltrates and their response to oHSV treatment involves the evaluation of cytokine expression changes and surface marker upregulation. However, limited immune infiltrates in some treated tumors can restrict phenotypic assessment and may introduce confirmation bias into studies. This may also limit contextualized or integrated assessment of immune response changes and increases the need for repeated expensive animal studies for complete characterization. Techniques like single-cell RNA sequencing and mass cytometry offer multiparameter assessments but are relatively expensive and require specialized equipment and expertise, limiting their accessibility in some research settings. Spectral flow

Received 4 October 2024; accepted 18 December 2024;
https://doi.org/10.1016/j.omton.2024.200929.

[5]These authors contributed equally

Correspondence: Kevin A. Cassady, Center for Childhood Cancer Research, Abigail Wexner Research Institute at Nationwide Children's Hospital, Columbus, OH, USA.
E-mail: kevin.cassady@nationwidechildrens.org

cytometry overcomes some of these challenges by providing a high-dimensional immune cell analysis that improves the depth and sensitivity of tumor-infiltrating leukocyte (TIL) analysis.

Here, we developed a 46-parameter spectral cytometry panel that can characterize both the lymphoid and myeloid compartments and includes intracellular cytokine and transcription factor (FOXP3) staining for immune functional assessments. This staining panel provides sufficient sensitivity for detecting immune cell changes, applicable not only in leukocyte-rich samples (e.g., peripheral blood, bone marrow, lymphoid organs) but also in environments with limited leukocyte presence (e.g., tumors). In this study, we demonstrated its utility in evaluating immune effector changes following oHSV treatment combined with the FDA-approved JAK protein kinase inhibitor ruxolitinib (RUX). We previously demonstrated that RUX+oHSV combination therapy reduced murine sarcoma growth, prolonged survival, and increased activated CD8(+) T cell frequency, shifting the cytotoxic T cell-to-regulatory T cell (Treg) ratios within tumors early post-treatment.[7] We also explored how the loss of CD8(+) T cells impaired RUX+oHSV therapeutic activity. Due to limited number of detectors in conventional flow cytometry and the small number of available leukocytes, these studies were restricted to evaluating the cytotoxic cellular response and Treg changes and did not fully examine CD4 functional changes or other immune compartments, such as B cells, natural killer (NK) cells, and myeloid cell subsets, or later immune cell changes after repeat oHSV treatment. To address this limitation, we used our new spectral flow panel to investigate delayed lymphoid and myeloid immune response changes post-tumor treatment. This approach provided a more comprehensive understanding of the immune landscape while overcoming limitations posed by variations in immune infiltrate abundance. Here, we introduce this spectral panel and show that RUX pretreatment followed by repeated oHSV MPNST treatment induces CD4(+) and B cell functional changes, suggesting that a complex and polyfunctional immunotherapeutic response contributes to RUX+oHSV therapy efficacy.[7]

RESULTS

Development of a spectral flow cytometry panel for assessing oHSV-related TIL changes

OV treatment alters the composition and function of TILs within a complex tumor microenvironment. To comprehensively evaluate the impact of oncolytic HSV (oHSV) on TIL activity following treatment, we developed a 46-color high-dimensional flow cytometry panel with minimal spectral overlap (similarity index ≤ 0.98) and optimized marker selection based on expression levels and fluorochrome brightness. A best-fit approach with commercially available antibodies was used due to the limited availability of certain combinations (Figure 1A; Table S1), and the panel was initially validated for spectral overlap and performance using antibody-binding beads.

Most antibodies demonstrated enhanced performance, with a greater than one logarithmic (log) difference in the mean fluorescence intensity (MFI) between positive and negative signals (Figure S1). Antibodies targeting interleukin (IL)-21, CD11b, CD5, major histocompatibility complex (MHC) class II, CD62L, Siglec-5, and GL-7 displayed $\geq$half-log differences. These smaller MFI differences, however, still provided reliable positive peaks suitable for cellular staining applications.

Next, we conducted serial dilution experiments (1:400–1:2,000) to determine the optimal antibody concentrations for staining leukocyte subpopulations. Splenocytes were used for initial evaluations, with bone marrow cells and peripheral blood cells (PBCs) (Figure 1B) used in subsequent experiments to refine antibody concentrations for improved B cell phenotype discrimination. Stimulation with phorbol 12-myristate 13-acetate (PMA) and ionomycin in the presence of a Golgi block allowed the assessment of antibodies against activation markers (CD25, CD44, and CD69) and intracellular cytokines (tumor necrosis factor alpha [TNF-α], interferon [IFN]-γ, IL-4, IL-12, IL-17A, IL-21, granzyme B [GzB]). The highest dilution yielding a relatively high stain index (SI) was selected as the optimal concentration for each antibody (Figure S2).

Myeloid and lymphoid population assignments and gating strategy

Using validated antibody concentrations, we next implemented a comprehensive gating strategy to analyze PMA/ionomycin-stimulated splenocytes and fresh blood/bone marrow. Upon finalizing this gating strategy, we applied a similar approach to TILs. Forward- and side-scatter parameters were used to exclude debris and select viable leukocytes (Figure 2A). Viable CD45(+) cells were further identified using low Zombie NIR viability stain and high CD45 expression.

Within the live CD45(+) population, we categorized CD19(+) B cells into regulatory (Bregs) and effector subsets, such as transitional cells, marginal zone (MZ) cells, follicular (FOL) cells, germinal center (GC) cells, PBs, and PCs, based on specific markers (Table 1).[8–13] B1 cells were characterized among CD19(+)B220(−) populations.[14] B cell activation was characterized by evaluating the expression levels (MFI) of CD80, CD86, MHC class II, and CD69.[13]

Among CD19(−) cells, NK cells, T cells (CD3[+]), and NKT cells were identified.[15,16] T helper (CD4[+]) and cytotoxic (CD8[+]) T cells were distinguished within T cells. Tregs were identified by FOXP3 expression in CD4(+) cells. Both CD4(+) and CD8(+) T cells were also analyzed for surface markers (Ly6C, CD44, CD62L, CD49b, CD103, CD25, CD69) and intracellular cytokines (TNF-α, IFN-γ, IL-4, IL-17A, IL-21, GzB). PD-1 expression on T cells was analyzed as an early activation marker or an indicator of potential exhausted phenotypes.[17] Classification of CD44 and CD62L expressions allowed categorization of CD44(−), CD62L(+) naive, CD44(+)CD62L(+) central memory (TCMs), and CD44(+) CD62L(−) effector/effector memory (T_{EFF}/T_{EM}) T cells.[18] CD103 expression identified tissue-resident memory T (TRM) cells,[19,20] and their activation was evaluated by CD25 and CD69 expression.[21]

Myeloid cells were gated on CD19(−)CD3(−)NK1.1(−)CD93(−) CD138(−) populations, followed by specific marker gating (Table 1).[22–28] The activation of myeloid cells was defined by CD80,

A

Fluor	Target	Fluor	Target	Fluor	Target	Fluor	Target	Fluor	Target
BUV395	CD103	eFluor 450	Ly6C	BB515	CD8α	RB744	MHC-I	cF BYG750	MHC-II
BUV496	NK-1.1	BV480	CD28	FITC	HSV gD	RB780	CD19	PE/Cyanine7	CD93
BUV563	F4/80	BV510	IL-17A	S Blue 550	B220	PE	IgM	PE/Fire 810	CD3
BUV615	CD23	BV570	CD11b	NFB 585	CD62L	Spark YG 593	CD44	APC	IFN-Y
BUV661	CD86	BV605	PD1	NFB 610-70S	Siglec F	PE/Daz 594	CD25	AF 647	FOXP3
BUV737	CD49b	BV650	CD80	NFB 660-120S	CD5	PE/Fire 640	CD11c	S NIR 685	IgD
BUV805	CD1d	BV711	IL-4	PerCP	CD45	PE/Cyanine5	CD69	AF 700	IL-12
BV421	GzB	BV750	TNF-α	PerCpcy5.5	GL7	NFY 690	PDL1	APC-H7	CD4
AF405	IL-21	BV785	CD138	PerCP-ef710	TCR γδ	PE/Fire700	CD206	APC/Fire 810	Ly-6G

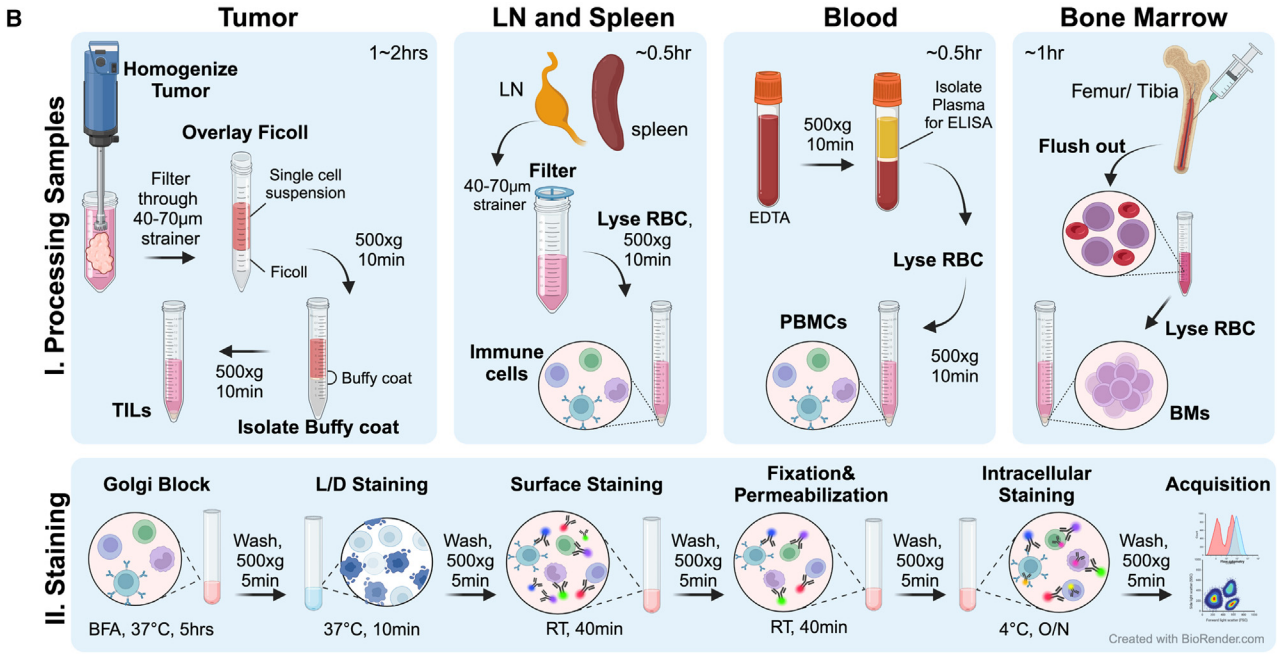

Figure 1. Preparation of single-cell suspension from blood and tissues for spectral flow staining

(A) Complete list of antibodies used in designing the spectral panel. (B) Schematic diagram illustrating the protocol for isolating leukocytes from tumors, lymph nodes (LNs), spleen, blood, and bone marrow. The single-cell suspension was incubated with a Golgi block (brefeldin A) with or without PMA/ionomycin at 37°C for 5 h. The cells were washed at 500 × *g* for 5 min with PBS and stained for live/dead (L/D) at 37°C for 10 min. Following washing with FACS buffer (PBS, 5% FBS, 0.01% NaN3), the cells were stained for surface markers for 40 min at room temperature (RT) using antibodies listed in (A). Samples were washed again, fixed, and permeabilized using FoxP3 fixation/permeabilization buffer and stained overnight (O/N) for intracellular targets at 4°C. Samples were washed and acquired using a spectral flow cytometer. The diagram was created with BioRender.com. NFB, NovaFluor Blue; NFY, NovaFluor Yellow; AF, Alexa Fluor; S NIR, Spark NIR; cF, cfluor; S Blue, Spark Blue. L/D differentiation with Zombie NIR (BioLegend).

CD86, and MHC class II expression, with PD-L1 indicating inhibitory signaling.[29,30] These markers were quantified using MFI to assess cellular activation, antigen presentation, or suppression of T cell activity. Frequencies of specific marker-expressing cell populations were expressed as percentages of their parent population or total CD45(+) cells.

RUX+oHSV treatment reduces myeloid cell populations in tumors

Our previous study demonstrated enhanced CD8(+) T cell activity with RUX preconditioning and C134 oHSV therapy.[7] We used this model as a reference in the current study to validate our multiparameter flow cytometry panel and investigate immune changes, especially after repeated oHSV dosing. Mice bearing established tumors ($n = 8$ per cohort) were treated with PBS or RUX (60 mg/kg) for three consecutive days, followed by two doses of PBS or C134 (3×10^7 PFU) 1 week apart (Figure 2B). Four days after the final oHSV treatment (day 11 post-initial oHSV treatment), TILs were incubated for 5 h in the presence of a Golgi plug, stained for surface markers and intracellular targets, and analyzed by spectral flow cytometry.

Immune infiltrate increased but absolute myeloid cell numbers remained constant following RUX+oHSV therapy (Figures 3A–3C).

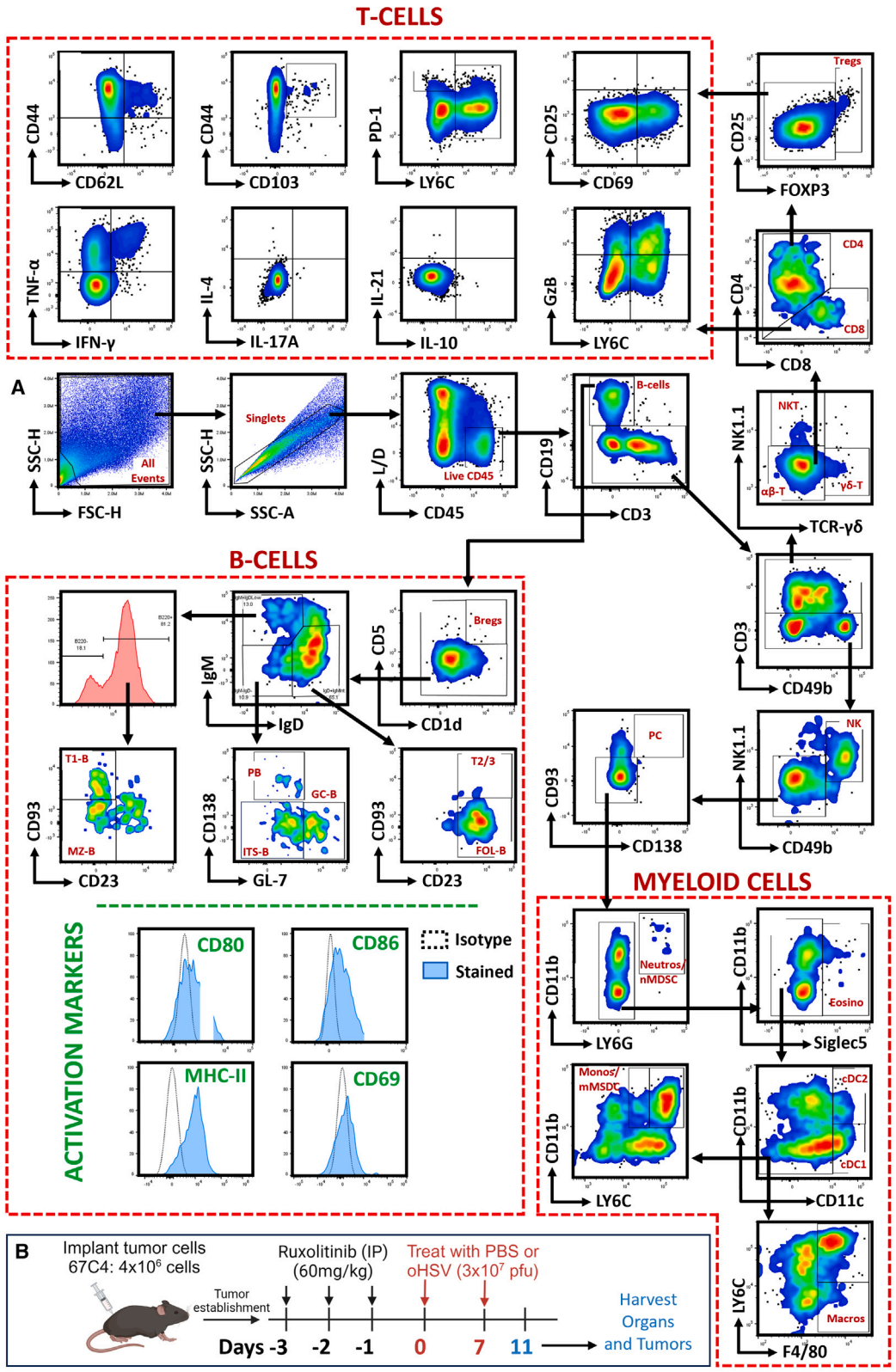

(legend on next page)

However, the relative myeloid abundance (40% in PBS-treated tumors) decreased proportionally (20% in RUX+oHSV-treated tumors) and was related to the lymphocyte influx after oHSV therapy (Figures 3D and S3A). This proportional decrease in myeloid cells was consistent across subsets such as Ly6G(+) granulocytes/myeloid-derived suppressor cells (MDSCs) (Figures 3E and S3B) and F4/80(+) macrophages (Figures 3F and S3C). Ly6C^{HI} inflammatory monocytes (Figures 3G and S3D), Siglec-F(+) eosinophil (Figure 3H), and CD11c(+) dendritic cell (data not shown) populations did not change significantly between treatment groups. These findings suggest that RUX pretreatment potentially plays a significant role in reducing the frequency and absolute number of immunosuppressive myeloid cells within the tumor microenvironment.

Both CD4(+) and CD8(+) T cells are activated and have a pro-inflammatory and polyfunctional effector phenotype in RUX+C134-treated tumors

Because T cell populations increased post-RUX+C134 treatment, we anticipated that both T helper and cytotoxic T cell populations were equally responsible for this large lymphocyte infiltrate. RUX+C134 treatment increased the absolute number of both CD4 and CD8 populations (Figures S4A and S4B), predominantly the CD4(+) population, leading to an increase in CD4(+) frequency and a subsequent CD4:CD8 ratio increase (Figure 4A). Notably, other lymphoid populations, such as NKT and NK cells, remained unaffected in their proportions, numbers, and functions (Figures S4C–S4F).

Consistent with our prior findings,[7] RUX+oHSV treatment increased effector (T_{EFF}) or effector memory (T_{EM}) phenotypes with a subsequent decrease in the naive population within the CD8 compartment (Figures 4B and S4G). There was also an increase in Ly6C and GzB, both single and co-expressions (Figures 4C–4F), within these CD8(+) T cells, indicative of an improved pro-inflammatory and cytotoxic profile.[31,32] Consistent with this improved activity, they also exhibited increased expression of CD69 and CD28, suggestive of recent activation (Figures 4G, S4H, and S4I).

Similarly, RUX+C134 treatment amplified CD4(+) T cell infiltration within tumors, displaying a T_{EFF}/T_{EM} phenotype with reduced naive cell markers (Figure 4H). Like the pro-inflammatory CD8(+) T cells, these CD4(+) T cells exhibited higher Ly6C expression and lower PD-1 levels (Figure 4I), indicative of enhanced pro-inflammatory activity and a reduced likelihood of exhibiting an exhausted phenotype. Furthermore, increased CD69 (Figures 4J and S4J) and CD28 expression (Figure 4K) supported their activated status. Conversely, RUX+C134 decreased FOXP3(+) Tregs (Figure 4L), indicating a shift in the activation-inhibition immune balance toward enhanced effector functions after repeat oHSV dosing.

Next, we examined CD4(+) T cell cytokine and effector profiles to identify how RUX+oHSV altered CD4(+) T cell function. Intratumoral CD4(+) T cells were incubated in the presence of a Golgi block without exogenous stimulating agents for 5 h and stained for cytokines (IFN-γ, TNF-α, IL-4, IL-10, IL-17A, and IL-21) and GzB. Functionally active CD4(+) T cells expressing cytokines or GzB represented 2.97%–32.14% of total intratumoral CD4 infiltrates. oHSV treatment increased the frequencies of functionally active CD4(+) T cells compared to mock treatment (Figures 4M and S4K), with a decreased anti-inflammatory-to-pro-inflammatory ratio (Figure S4L) and no significant difference between the treatment groups when anti-inflammatory cytokines like IL-4 and IL-10 were examined individually (Figure S4M). Likewise, pro-inflammatory cytokines IL-17A and TNF-α also did not differ significantly (Figures 4N and S4N). Pretreatment with RUX significantly increased GzB-expressing CD4+ T cells to 17.76% ± 4.84% (absolute count: 1,044 ± 442) compared to 13.58% ± 3.94% (absolute count: 508 ± 371) observed with oHSV treatment alone (Figure 4O). This combination therapy resulted in a nearly 2.5-fold increase in the percentage and a 21-fold increase in the absolute count of these cells relative to the Rux+PBS control group (Figure 4O). Similarly, the Rux+C134 treatment significantly elevated IFN-γ-expressing CD4+ T cells by approximately 2-fold in percentage and 8-fold in absolute count compared to PBS-treated tumors (Figures 4O and S4O). These findings indicate that Rux and C134 together promote the differentiation of CD4+ T cells toward cytotoxic-like Th1 phenotypes. Moreover, increased IL-21(+)CD4(+) T cell populations (Figure S4P) suggested the potential involvement of follicular helper (Tfh)-like functions within the treated tumors. In summary, the spectral staining results reinforce our previous observation that RUX+oHSV treatment increases T_{EFF}/T_{EM} populations and activity within the tumor and show that this is not limited to CD8 T cell activity but also involves a large CD4 influx with increased activity.[7]

Figure 2. Flow gating strategy and experimental design

(A) Gating strategy on acquired samples was performed using FlowJo v.10.8.1. Cellular debris and dust particles were excluded using forward- (FSC) and side-scatter (SSC) parameters. Singlets and viable CD45(+) cells were selected. B cells (CD3[−]CD19[+]) were further phenotyped for their subsets. CD19(−) cells were gated for natural killer (NK) cells, plasma cells (PCs), and CD3(+) cells. CD3(+) cells were further characterized as NKT cells, γδ-T cells, or αβ-T cells. αβ-T cells were further distinguished as CD8(+) cytotoxic T cells, regulatory T cells (FoxP3+), or FoxP3(−)CD4(+) T helper cells. Both T cells were analyzed for surface markers (Ly6C, CD44, CD62L, CD49b, CD103, CD25, CD69, and PD-1) and intracellular cytokines (TNF-α, IFN-γ, IL-4, IL-17A, IL-21, granzyme B). Myeloid cells were gated on CD19(−)CD3(−)NK1.1(−)CD93(−)CD138(−) populations, followed by sequential specific markers to gate neutrophils/granulocytic myeloid-derived suppressor cells (gMDSCs), eosinophils, dendritic cells, monocytes/monocytic MDSCs (mMDSCs), and macrophages. Activation of B cells and myeloid cells was defined by measuring the mean fluorescence intensity (MFI) and proportions of CD80, CD86, CD69, and MHC class II expression. Frequencies of specific marker-expressing cell populations were expressed as percentages of their parent population or total CD45(+) cells. (B) Schematic of experimental design for murine tumor studies. Three- to four-week-old C57BL/6 mice were implanted subcutaneously with 4×10^6 67C-4 tumor cells per flank. When the tumor size reached 50–300 mm^3, mice were randomized, and the tumors ($n = 8$ per cohort) were treated with 3 doses of ruxolitinib (60 mg/kg) or PBS at −3, −2, and −1 day before PBS or oHSV (3×10^7) treatment on days 0 and 7. All mice were sacrificed on day 11 post-initial oHSV/PBS dose, and tumors and tissues were harvested and analyzed using spectral flow cytometry.

Table 1. Lineage markers to define intratumoral immune populations

Phenotypes	Markers used
Total B cells	CD19+CD3-CD11b-
Transitional B cells T1	CD19+IgM+IgDLowCD93+CD23-
Transitional B cells T2/T3	CD19+IgD+IgMIntCD93+CD23+
Marginal Zone B- cells (MZ-B)	CD19+IgM+IgDLowCD93-CD23-
Follicular B- cells (FOL-B)	CD19+IgD+IgMIntCD93-CD23+
Germinal Center B- cells	CD19+CD138-GL-7+
Plasmablasts	CD19+CD138+
Isotype Switched B- cells (ITS-B)	CD19+IgD-IgM-
Plasma Cells	CD19−CD3−CD49b−NK1.1−CD93+CD138+
B1 cells	B220−CD19+CD23−CD5+(B1a)/CD5−(B1b)
Regulatory B cells	CD19+CD1d+CD5+
Mature NK	CD49b+NK1.1+
NKT cells	CD3+NK1.1+
T cells	CD3+ (CD4+Th/CD8+Tc)
Tregs	CD4+FoxP3+
Neutrophils	CD11b+Ly6G+
Eosinophils	CD11b+Siglec5+
Monocytes	CD11b+Ly6Chi/lo
Macrophages	F480+
Plasmacytoid dendritic cells (DCs)	B220+CD11c+CD11b−
Classical DCs	B220−CD11b+CD11c+
Lymphoid DCs	B220−CD3−CD8α+CD11c+

RUX+oHSV treatment increases activated GC-B cells in tumors

Next, we investigated RUX+oHSV treatment's impact on B cell populations in the tumor microenvironment. Absolute B cell numbers were similar between all treatment cohorts (Figure 5A), but CD19(+) B cell frequency decreased in RUX+C134-treated tumors compared to other treatments and was related to the large T cell influx in this treatment cohort. The B cell subpopulations differed between treatment groups, which suggests different functional effects between the treatment groups.

Our multiparameter panel can discriminate between transitional (T1/T2/T3) B cells, FOL-B cells, MZ-B cells, GC-B cells, PBs, and PCs. In all treatment cohorts, FOL-B cells formed the majority B cell subgroup, comprising 69%–93% of the total B cell population (Figure 5B). CD5(+)CD1d(+) Bregs were lower in RUX+C134-treated tumors (Figure S4Q), whereas MZ-B cells, PBs, PCs, and isotype-switched (ITS) B cells did not differ between the treatment groups (data not shown). B1 cells (CD19[+]IgM[+]IgD^{low}B220[−]CD5[+]*B1a*/CD5[−]*B1b*) cells were absent in all the tumors (Figure S5A) and therefore excluded from this study. Notably, RUX+C134 treatment increased both the absolute number and frequency of B cells expressing GL7 (Figure 5C), a marker of functional GCs in secondary lymphoid tissues.[12,33,34] There was also increased costimulatory (CD80, CD86) and activation (CD69) surface expression on the B cells isolated from the RUX+C134-treated tumors compared to the oHSV-treated tumor samples (Figures 5D, 5E, S5B, and S5C), suggesting increased activity. MHC class II expression levels (Figure S5D) and frequency (data not shown) did not differ between C134- and RUX+C134-treated tumors.

DISCUSSION

Oncolytic virotherapy mediates its therapeutic effects through direct viral infection and lysis of infected tumor cells, as well as indirect immune-mediated activity induced by the virus. Tumors with relatively higher baseline levels of immune cell infiltrates typically show a further increase in immune activity in response to oHSV therapy. However, other, colder tumors exhibit minimal immune infiltrates even after virotherapy. Analyzing immune responses in such cold tumors is challenging due to the limited number of cells available to study using conventional flow cytometry, which allows for only a limited numbers of parameters to be assessed simultaneously. This limitation necessitates either focusing on a single cell population or conducting multiple experiments to obtain a comprehensive phenotype profile of immune changes induced by virotherapy. To overcome this, we developed a 46-colored multiparametric spectral flow cytometry panel to comprehensively assess the immune cell landscape, even with limited tumor immune cells. To illustrate its utility, we used a tumor model in which we previously described how RUX alters oHSV intratumoral activity (viral replication and IFN-stimulated gene [ISG] expression), resulting in initial immune infiltrate changes. These prior studies were focused on CD8(+) and Treg population changes because of limited leukocyte numbers and the constraints of conventional flow cytometry.[7] Now, by developing this larger spectral panel, we can simultaneously characterize both the lymphoid and myeloid immune compartment changes, providing new insights into how RUX+oHSV therapy impacts the myeloid, CD4(+), and B cell compartments within the treated MPNST microenvironment.

Using this multiparameter panel, we again recapitulated the previously reported CD8/Treg changes and show that these changes persist beyond the initial viral treatment and remain evident even after repeated oHSV dosing. The spectral panel also demonstrated a more complex T cell and B cell immune response that was not recognized previously, where myelosuppressive populations proportionally decline as CD4(+) infiltrates predominate. The results also reveal that RUX+C134 therapy did not change dendritic cell populations at day 11 post-initial treatment. This contrasts with our recently published findings on IL-12-armed oHSV therapy, where the cytokine-expressing oHSV increased this antigen-presenting cell population and its activity.[35] Neither cytokine-armed or non-armed oHSV significantly impacted NK or NKT cell numbers or functions at later time points. Studies have shown that oHSV-induced NK cell responses are typically immediate and transient, peaking around day 3 post-treatment.[36–38] The lack of detectable changes at day 11 in our studies likely reflects the delayed timing of the analysis, missing these early, short-lived responses.

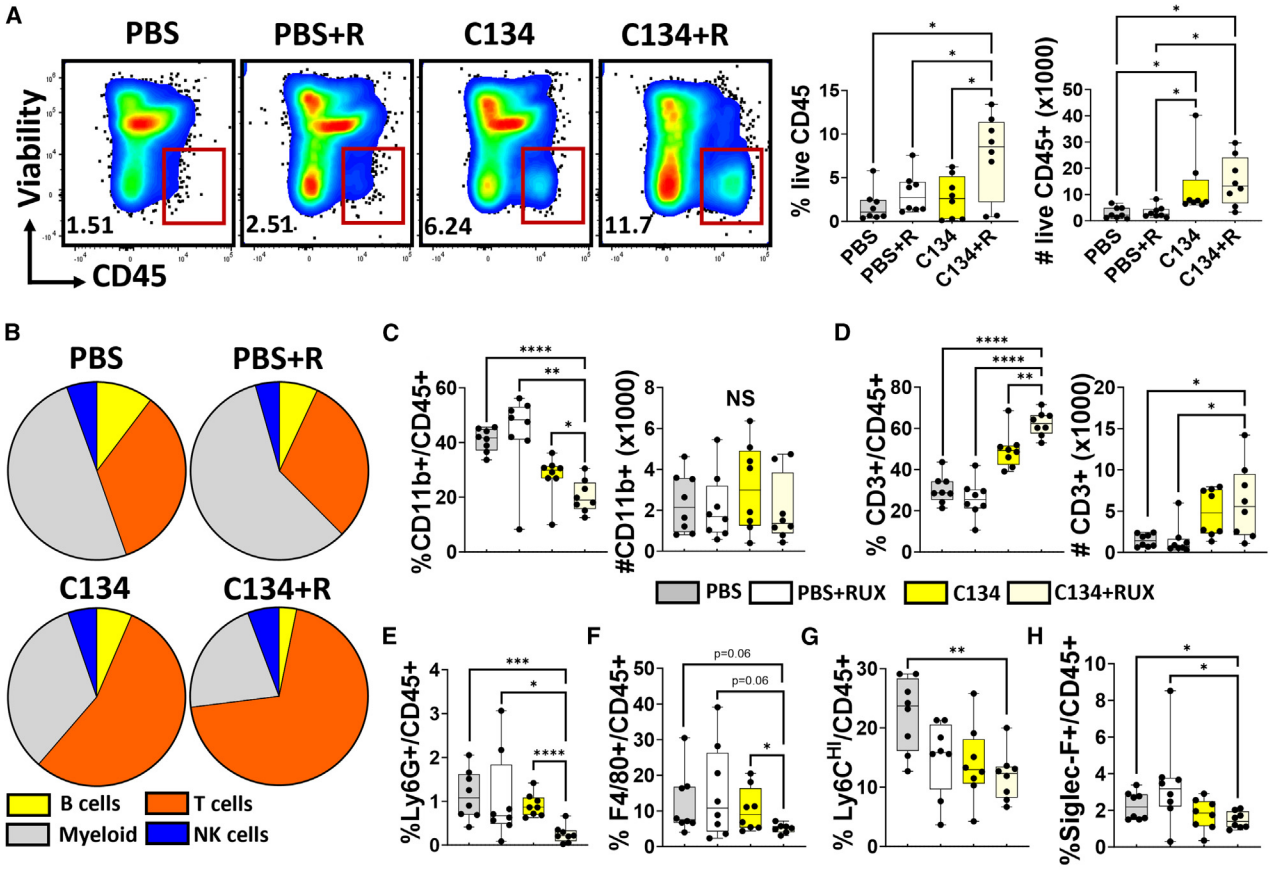

Figure 3. Intratumoral immune cell composition

Treated tumors ($n = 8$) were harvested on day 11 post-first dose of treatment. Tumor infiltrates were isolated, stained with fluorescent-labeled antibodies, and analyzed using spectral flow cytometry. (A) Representative flow plots, proportions, and absolute numbers of live CD45(+) immune cell infiltrates within tumors. (B) Pie charts showing the percentage compositions of B cells, T cells, myeloid cells, and NK cells within CD45(+) infiltrates. (C) Boxplot diagrams illustrate the proportions and absolute numbers of CD11b(+) myeloid cells among the different treatment groups. (D) Proportions and absolute numbers of NK1.1(−)TCRγδ(−)CD3(+) T cells within the treated tumors. (E) Proportions of CD11b(+)Ly6G(+) granulocytes/granulocytic myeloid-derived suppressor cells (gMDSCs) within treated tumors. (F) Differences in the proportions of F4/80(+) macrophages within treated tumors. (G) Proportions of intratumoral inflammatory monocytes. (H) Eosinophil proportions. Results are presented as box-and-whisker plots showing the median, with the 25th–75th percentile range as the box and the 5th–95th percentile as the whiskers. Dunn's post hoc analysis was done for multiple comparisons, with statistically significant values represented as $^{*}p < 0.05$, $^{**}p < 0.01$, $^{***}p < 0.001$, and $^{****}p < 0.0001$.

In our current study, virotherapy-treated tumors contained T cells with increased Ly6C surface expression. This upregulation occurred most consistently following RUX+C134 treatment and was also accompanied by greater activation marker expression, suggesting increased inflammatory activity.[31,32,39] While Ly6C is a classical monocyte marker, its expression in CD8(+) T cells correlates with pro-inflammatory traits and IFN-γ production.[31,32] The functional implications of Ly6C in CD4(+) T cells are less clear, although murine models show that it associates with increased GzB and IFN-γ expression during viral infections.[39] RUX+C134 treatment increased pro-inflammatory CD4(+) T cell effector infiltrates and CD4 activation while reducing Treg populations in the tumor environment. RUX+C134 also increased CD4(+) T cells that expressed GzB (cytolytic-like), IFN-γ (T helper type 1 [Th1]-like), and IL-21 (Tfh-like), indicative of a polyfunctional immune response.

GzB, a serine protease primarily associated with cytotoxic lymphocytes, such as NK cells and CD8(+) T cells, can also be expressed by activated CD4(+) T cells, conferring cytolytic capabilities.[40,41] Within tumors, GzB-expressing CD4(+) T cells constitute a significant proportion (∼2%–40%) of the total CD4(+) T cell population across various cancer types[42] and can lyse tumor cells.[43,44] Conversely, CD4(+)FoxP3(+) Treg populations can also contain GzB(+) populations that promote immune suppression.[45,46] In our C134+RUX-treated tumors, the CD4(+)GZB(+) population occurred within FOXP3(−)-gated samples, suggesting that they represent tumor-related cytolytic populations rather than suppressive functions. The higher frequencies of GzB(+)CD4(+) T cells observed in our study, alongside CD8(+) cells in the same locale, highlight CD4(+) T cells as a relevant source of GzB within tumors. Considering our observation of this increase in pro-inflammatory, polyfunctional

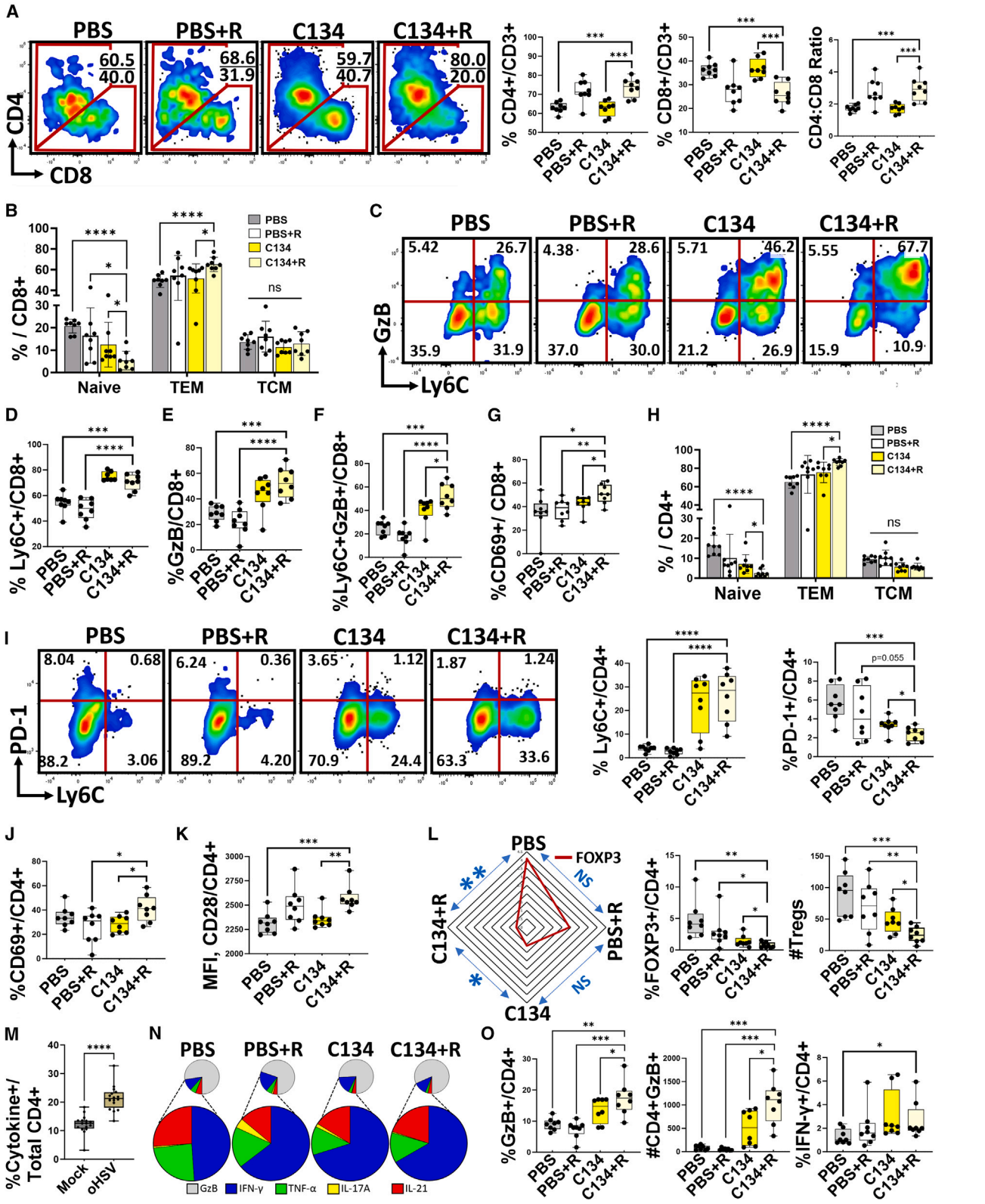

(legend on next page)

CD4(+) T effectors and CTLs, a decrease in Tregs, and the improved anti-tumor response, we postulate that these GzB-expressing CD4(+) T cells may contribute to tumor cytolytic activity. Future studies will investigate their specific contribution to the C134 therapeutic effect in tumors.

Our study revealed that RUX+C134 treatment significantly increased the population of Tfh-like cells and $GL7^{High}$ B cells with an activated phenotype within tumors compared to other treatment groups. These immune cell populations are typically associated with GC reactions in lymphoid tissues and tumors, where they play critical roles in B cell activation, maturation, and functions.[12,47–49] In this study, Tfh cells were present in all cohorts; however, their presence with activated GL7(+) B cells within the tumor microenvironment only occurred in the RUX+C134-treated cohort and suggests the possible formation of localized lymphoid-like structures, which could enhance local immune responses and contribute to the observed therapeutic efficacy in this sarcoma model.[50,51] However, definitive evidence of tertiary lymphoid structure formation in our murine syngeneic tumor models would require further spatial and temporal studies. The treatment-mediated differences in B cell phenotypes observed in this study may indicate enhanced B cell activity, including increased production of pro-inflammatory cytokines or tumor/virus-targeting antibodies in RUX+C134-treated mice. However, the study was designed to examine relatively early changes and focused on spectral panel validation. Serum or plasma sample collection from treated mice at later time points would also allow for a more comprehensive investigation of humoral response differences following this therapy.

This study also highlights the transformative potential of our multiparametric spectral flow cytometry panel. This advanced tool not only enables the detailed analysis of immune phenotypes within the tumor microenvironment but also holds broad applicability for studying immune responses in various other disease models in mice. By providing a comprehensive view of immune cell dynamics, this multiparameter panel provides a valuable tool for both investigators interested in tumor immunotherapy and other diseases that would benefit from immunological phenotyping, such as immune dysregulation and deficiency or organ transplant outcomes in murine models.[52,53] The panel was optimized for immune cells from C57Bl/6 mice, and its effectiveness in other mouse strains with different genotypes and potentially varying immune cell marker expression may require further antibody substitution and concentration adjustments. In conclusion, here we present a validated a 46-parameter spectral flow cytometry panel, confirming its accuracy by replicating results in a well-established tumor model. This panel uncovered previously unrecognized immune responses to RUX+oHSV therapy, highlighting the enhanced efficacy of this combination. The panel's demonstrated versatility extends its transformative potential across various cancer and disease models in mice, offering a powerful and cost-effective tool for advancing immune profiling.

MATERIALS AND METHODS

Cell lines and viruses

The murine MPNST line, 67C-4, was generously provided by Dr. Nancy Ratner (University of Cincinnati, Cincinnati, OH) and maintained in DMEM and 10% FBS. C134 is a $\Delta\gamma_1$34.5 virus derived from C101 that contains the HCMV IRS1 gene under control of the HCMV IE promoter in the UL3/UL4 intergenic region and was previously described.[54]

Animal tumor studies

Animal studies were approved by the Nationwide Children's Hospital Institutional Animal Care and Use Committee (IACUC, protocol no. AR19-00177) and performed in accordance with guidelines established by the Department of Defense and the National Institutes of Health (NIH) Guide for the Care and Use of Laboratory Animals. A flank 67C-4 MPNST model in C57BL/6 mice was chosen for this study. For the study, 3- to 4-week-old C57BL/6 mice were obtained from Envigo (Frederick, MD) and implanted subcutaneously with 4×10^6 cells in 50 μL of phosphate-buffered saline (PBS)/flank. Tumor sizes were measured biweekly by caliper after implantation, and tumor volume was calculated by length × width × height. Similar to our previous study, animals were randomized into treatment groups when tumors reached 50–300 mm^3 in size and treated with 3 doses of RUX (INCB018424, ApexBio; 60 mg/kg) or PBS intraperitoneally (i.p.) each day prior to PBS or oHSV C134 (3×10^7 PFU in 50 μL PBS/flank) treatment intratumorally (ITu). Tumors were injected with PBS or oHSV (3×10^7 PFU in 50 μL PBS/flank) a second time 7 days following the first treatment. Mice were sacrificed at day 11 following the first oHSV treatment (day 4 after the second

Figure 4. Tumor-infiltrating T cell frequencies, phenotypes, activation status, and functions

Treated tumors ($n = 8$) were harvested and tumor cells isolated and stained with fluorescent-labeled antibodies to analyze using spectral flow cytometry. (A) Differences in the proportion and ratio of CD4(+) and CD8(+) T cells among PBS- and oHSV-treated tumors. (B) Proportional differences of CD44(−)CD62L(+) naive, CD44(+)CD62L(−) effector/effector memory (T_{EFF}/T_{EM}), and CD44(+)CD62L(+) central memory (TCM) phenotypes of intratumoral CD8(+) T cells among the treatment groups. (C) Representative flow plots showing the expression of Ly6C and granzyme B (GzB) on CD8(+) T cells. (D) Proportions of total Ly6C-expressing CD8(+) T cells. (E) Proportions of total GzB-expressing CD8(+) T cells. (F) Proportions of both Ly6C- and GzB-expressing CD8(+) T cells. (G) Proportions of CD8(+) T cells expressing early activation marker CD69. (H) Proportional differences of naive, TCM, and T_{EFF}/T_{EM} phenotypes of intratumoral CD4(+) T cells among the treatment groups. (I) Representative flow plots and proportions of intratumoral CD4(+) T cells expressing pro-inflammatory marker Ly6C and a marker of potential exhaustion, PD-1, among different cohorts. (J) Proportions of activated CD4(+) T cells from treated tumors. (K) Intensity of CD28 expression within CD4(+) T cells on a single-cell basis, measured by mean fluorescence intensity (MFI). (L) Proportion and absolute number of FOXP3(+) regulatory T cells (Tregs) within tumors among treated groups. (M) Proportions of cytokine-expressing CD4(+) T cells. (N) Pie chart showing the percentage composition of CD4(+) T cells expressing GzB, interferon-γ (IFN-γ), tumor necrosis factor alpha (TNF-α), interleukin-17A (IL-17A), and IL-21 among the total CD4(+) tumor infiltrates. (O) Proportions and absolute numbers of intratumoral CD4(+) T cells expressing GzB and INF-γ. Statistically significant values are represented as $^*p < 0.05$, $^{**}p < 0.01$, $^{***}p < 0.001$, and $^{****}p < 0.0001$.

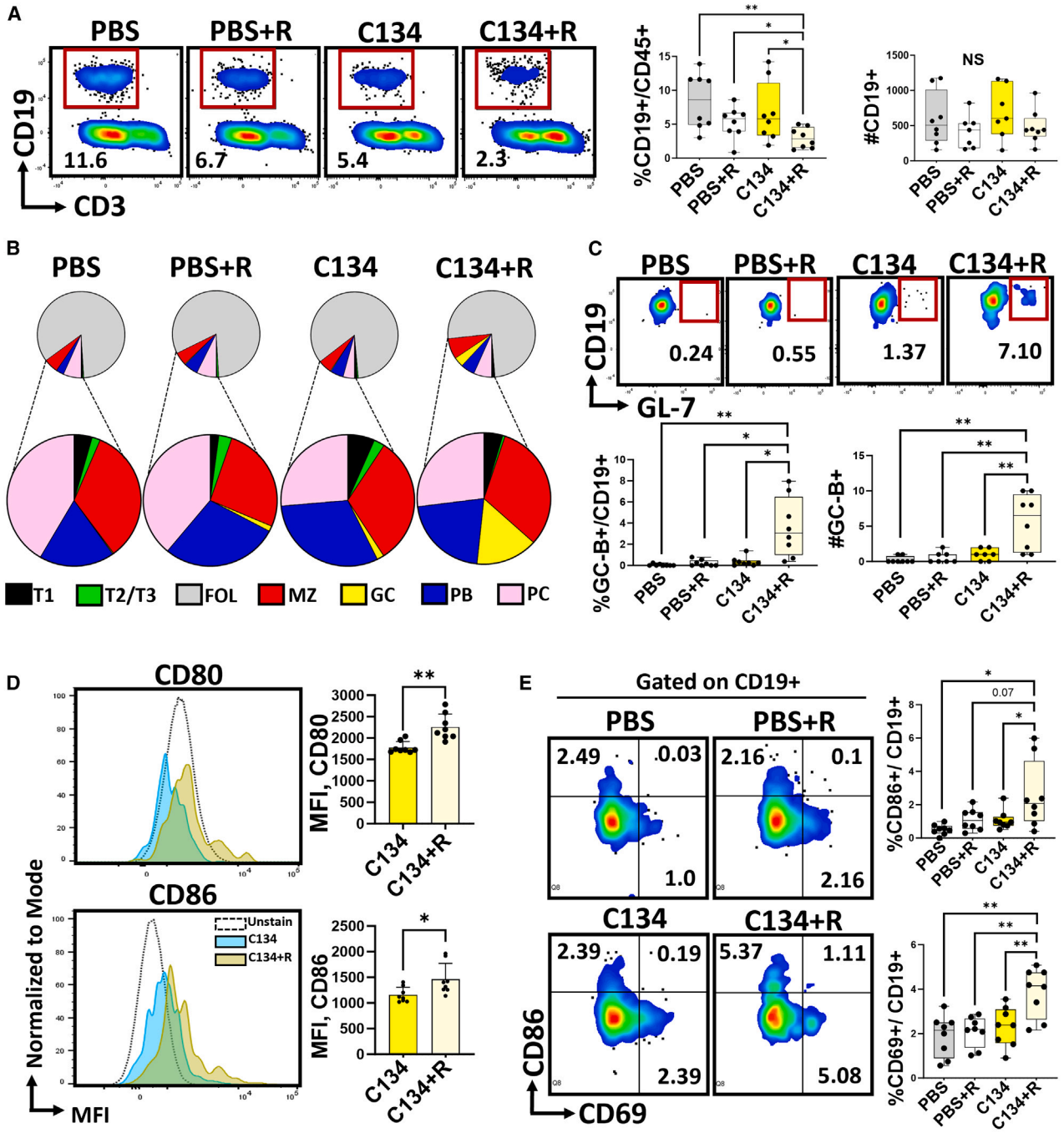

Figure 5. Tumor-infiltrating B cell numbers, their phenotypes, and activation status

Treated tumors ($n = 8$) were harvested and tumor cells isolated and stained with fluorescent-labeled antibodies to analyze using spectral flow cytometry. (A) Representative flow plots, proportions, and absolute numbers of CD19(+) total B cells within the treatment groups. (B) Pie chart showing the percentage composition of B cell phenotypes: transitional (T1/T2/T3), follicular (FOL), marginal zone (MZ), germinal center (GC), plasmablasts (PBs), and plasma cells (PCs) among total immune infiltrates within the treated tumors. (C) Representative flow plots, proportions, and absolute numbers of GL7(+) GC-B cells within the tumors. (D) Differences in the mean fluorescence intensity (MFI) of CD80 and CD86 expression between C134 and C134+RUX treatments. (E) Representative flow plots and proportions of B cells expressing B cell activation markers CD69 and CD86. Statistically significant values are represented as $^{*}p < 0.05$, $^{**}p < 0.01$, $^{***}p < 0.001$, and $^{****}p < 0.0001$.

oHSV dose). Tumors were harvested and processed immediately for phenotyping.

Isolation of blood cells, splenocytes, bone marrow cells, and tumor infiltrates

Flow panel optimization was performed using peripheral blood, splenocytes, or bone marrow cells. Following optimization, tumor infiltrates were used as samples for comprehensive phenotyping in this study.

Peripheral blood collection

Peripheral blood was obtained through direct cardiac puncture using a 30G needle and 1 mL syringe following the protocol outlined previously.[55] In brief, blood was collected in EDTA vacutainers and immediately placed on ice. Samples were transferred to 15 mL conical tubes, treated with 3 mL of red blood cell lysis buffer (ACK, Gibco, Waltham, MA) for 10 min at room temperature, washed with 7 mL of media, and finally resuspended in 1 mL of media for further processing.

Splenocyte isolation

Spleens were collected in a 5 mL plastic tube containing RPMI and 10% FBS on ice and were mechanically dissociated by passing them through a 70 μm cell strainer using a sterile 5 mL syringe plunger. Splenocytes were washed and treated with ACK lysis buffer as described for peripheral blood, washed, and finally resuspended in FBS+10% DMSO. Aliquots of 1 mL containing 10 million cells/vial were stored at −80°C for 72 h in a Mr. Frosty freezing container (Thermo Fisher Scientific, Waltham, MA) before being transferred to liquid nitrogen for long-term storage.

Bone marrow isolation

Bone marrow was isolated from the tibias and femurs of mice as previously described.[56] Briefly, bones were collected in 5 mL RPMI and 10% FBS, transported on ice, and the marrow was flushed out into a sterile Petri dish. The cells were collected, treated with ACK lysing solution, washed, and resuspended in the required volume of media for immediate processing in flow cytometry experiments.

Tumor infiltrate isolation

Flank tumors were harvested and homogenized by mechanical disruption using scissors and the TissueRuptor II (Qiagen). The homogenized samples were passed through a 70 μm cell strainer and pelleted, and leukocytes were separated by Ficoll (Ficoll-Paque PREMIUM 1.084, Cytiva, Marlborough, MA) overlay. The leukocyte buffy coat was isolated, washed, and reconstituted in the required volume of media for flow cytometry staining.

Staining of cells for flow cytometry

Flow panel optimization was initially performed using frozen splenocytes, freshly isolated PBCs, or bone marrow cells from tumor-bearing mice. Fresh tumor infiltrates were then characterized with the optimized panel. On the day of staining, frozen splenocytes were thawed, washed, and resuspended in RPMI with 10% FBS. Approximately 2×10^6 cells (splenocytes, PBCs, or bone marrow cells) or leukocytes from whole tumors were transferred into 5 mL round polypropylene tubes (Falcon, Durham, NC) for staining with fluorochrome-conjugated antibodies.

For studies involving intracellular cytokine and cell activation, cells were stimulated with a cocktail of PMA and ionomycin (eBiosciences, San Diego, CA) for 1 h, followed by the addition of brefeldin A (eBioscience, San Diego, CA). Subsequently, cells were incubated for an additional 5 more hours at 37°C with 5% CO_2. Post-stimulation, cells were washed and incubated with Zombie NIR fixable viability dye (BioLegend) at a 1:1,000 dilution for 20 min at 37°C. Fc receptors on cells were blocked for 15 min with anti-mouse CD16/CD32 (eBiosciences, San Diego, CA). Surface staining was carried out by incubating cells with 300 μL of appropriately diluted single antibody (for dilution experiment) or combinations of anti-mouse antibodies (full panel) for 40 min at room temperature in the dark. Following washing, cells were fixed and permeabilized using the FoxP3/transcription factor staining buffer set (eBiosciences).

For intracellular staining, fixed-permeabilized cells were treated with 300 μL of appropriately diluted antibodies targeting intracellular cytokine(s) or transcription factor(s) overnight at 4°C. Samples were washed the following day and resuspended in 300 μL of fluorescence-activated cell sorting (FACS) buffer (PBS+5%FBS+0.01% sodium azide). Data acquisition was performed using a Cytek Aurora spectral flow cytometer with five lasers (355, 405, 488, 561, and 640 nm) and 64 detectors, employing SpectralFlo v.3.1.0 (Cytek Biosciences, Fremont, CA). The acquired data were analyzed using FlowJo v.10.8.1 (BD Biosciences, Franklin Lakes, NJ). Markers of interest were expressed either as a percentage of the parent cell population or as absolute event counts. Gates were assigned by comparison to samples stained with antibodies using the fluorescence-minus-one method for cytokines as an assessment for nonspecific binding.

Panel design, antibody list, and working concentration of antibodies

A multiparametric spectral flow panel capable of detecting functional changes in the myeloid and lymphoid compartments using surface and intracellular staining was developed using the antibodies specific to lineage markers, activation, inhibition, memory phenotypes, cytokines, and transcription factors.

First, using the similarity index (Cytek Biosciences), we selected 46 fluorochromes with minimal spectral overlap. Fluorochromes were assigned to markers based on cellular expression levels, with brighter fluorophores paired with low-expressing markers.

Antibodies were obtained from BD Biosciences, BioLegend, Thermo Fisher Scientific, R&D Systems (Minneapolis, MN), and Bio-Rad Laboratories (Hercules, CA). Antibody performance was tested using immunoglobulin isotype-independent spherical beads (Invitrogen, Carlsbad, CA), ensuring appropriate laser excitation and emission detection of the antibodies.

Optimal antibody concentrations were determined by serial dilutions (1:400 to 1:2,000) tested on splenocytes, blood, and bone marrow cells. PBCs were mixed with bone marrow cells in a 1:1 ratio to test antibodies specific for B cell phenotypes. Cells were stimulated with PMA and ionomycin to assess the optimum dilution of antibodies targeting cytokines and activation/exhaustion markers. Unstained cells served as the "no-antibody" control. The SI was calculated using FlowJo v.10.8.1, and higher dilutions with optimal SIs were selected for the panel.

Statistical analysis

Differences in the frequencies and absolute quantities of cells expressing specific markers among treated and non-treated cohorts were compared with one-way ANOVA or a Student's t test. To control for type I error, the Benjamini-Hochberg method was employed for adjusting multiplicities related to primary hypotheses. Adjusted $p < 0.05$ was considered significant. All statistical analyses were performed using Prism GraphPad v.10.1.0 (GraphPad Software, San Diego, CA). Statistical significance was designated with asterisks as follows: $*p < 0.05$, $**p < 0.01$, $***p < 0.001$, and $****p < 0.0001$.

DATA AND CODE AVAILABILITY

The datasets generated and analyzed during the current study are included within this article and its supplemental information. Any additional inquiries can be directed to the corresponding author.

ACKNOWLEDGMENTS

This work was funded by the Department of Defense (W81XWH2010340 and NF180126), the NIH (R01CA222903, U54CA232561, U54CA232561-01A1S5, and T32CA269052), and CancerFree KIDS (CFK). We extend our gratitude to the veterinarians and Animal Resource Core staff at Nationwide Children's Hospital for their diligent care of the mice used in this research. We also acknowledge Cecele Denman and Dave Dunaway from the Flow Core at Nationwide Children's Hospital for their assistance with the spectral flow cytometry acquisition.

AUTHOR CONTRIBUTIONS

R.D. conceived the project, performed the experiment and analyses, created the figures, and drafted the manuscript. Y.K. conducted the experiment and drafted, reviewed, and edited the manuscript. D.K. prepared the figures and drafted, reviewed, and edited the manuscript. I.H.-A., J.H., and A.M. assisted with *in vivo* experiments and reviewed and edited the manuscript. K.A.C. conceptualized the study, provided funding, supervised the study, and reviewed and edited the manuscript.

DECLARATION OF INTERESTS

K.A.C receives licensure payments from Mustang Bio (Worcester, MA) for the C134 virus, though there are no relevant financial conflicts related to the technology addressed in this paper.

SUPPLEMENTAL INFORMATION

Supplemental information can be found online at https://doi.org/10.1016/j.omton.2024.200929.

REFERENCES

1. Fuchs, B., Spinner, R.J., and Rock, M.G. (2005). Malignant peripheral nerve sheath tumors: an update. J. Surg. Orthop. Adv. *14*, 168–174.
2. Bates, J.E., Peterson, C.R., Dhakal, S., Giampoli, E.J., and Constine, L.S. (2014). Malignant peripheral nerve sheath tumors (MPNST): a SEER analysis of incidence across the age spectrum and therapeutic interventions in the pediatric population. Pediatr. Blood Cancer *61*, 1955–1960. https://doi.org/10.1002/pbc.25149.
3. Uusitalo, E., Rantanen, M., Kallionpää, R.A., Pöyhönen, M., Leppävirta, J., Ylä-Outinen, H., Riccardi, V.M., Pukkala, E., Pitkäniemi, J., Peltonen, S., and Peltonen, J. (2016). Distinctive Cancer Associations in Patients With Neurofibromatosis Type 1. J. Clin. Oncol. *34*, 1978–1986. https://doi.org/10.1200/JCO.2015.65.3576.
4. Paudel, S.N., Hutzen, B., and Cripe, T.P. (2023). The quest for effective immunotherapies against malignant peripheral nerve sheath tumors: Is there hope? Mol. Ther. Oncolytics *30*, 227–237. https://doi.org/10.1016/j.omto.2023.07.008.
5. Fridman, W.H., Zitvogel, L., Sautès-Fridman, C., and Kroemer, G. (2017). The immune contexture in cancer prognosis and treatment. Nat. Rev. Clin. Oncol. *14*, 717–734. https://doi.org/10.1038/nrclinonc.2017.101.
6. Sobczuk, P., Teterycz, P., Czarnecka, A.M., Świtaj, T., Koseła-Paterczyk, H., Kozak, K., Falkowski, S., and Rutkowski, P. (2020). Systemic Treatment for Advanced and Metastatic Malignant Peripheral Nerve Sheath Tumors-A Sarcoma Reference Center Experience. J. Clin. Med. *9*, 3157. https://doi.org/10.3390/jcm9103157.
7. Ghonime, M.G., and Cassady, K.A. (2018). Combination Therapy Using Ruxolitinib and Oncolytic HSV Renders Resistant MPNSTs Susceptible to Virotherapy. Cancer Immunol. Res. *6*, 1499–1510. https://doi.org/10.1158/2326-6066.CIR-18-0014.
8. Yanaba, K., Bouaziz, J.D., Haas, K.M., Poe, J.C., Fujimoto, M., and Tedder, T.F. (2008). A regulatory B cell subset with a unique CD1dhiCD5+ phenotype controls T cell-dependent inflammatory responses. Immunity *28*, 639–650. https://doi.org/10.1016/j.immuni.2008.03.017.
9. Willis, S.N., Tellier, J., Liao, Y., Trezise, S., Light, A., O'Donnell, K., Garrett-Sinha, L.A., Shi, W., Tarlinton, D.M., and Nutt, S.L. (2017). Environmental sensing by mature B cells is controlled by the transcription factors PU.1 and SpiB. Nat. Commun. *8*, 1426. https://doi.org/10.1038/s41467-017-01605-1.
10. Khalil, M., Ray, A., and Dittel, B.N. (2021). Characterization of the Cell Surface Phenotype and Regulatory Activity of B-Cell IgD Low (BD(L)) Regulatory B Cells. Methods Mol. Biol. *2270*, 217–231. https://doi.org/10.1007/978-1-0716-1237-8_12.
11. Noviski, M., Mueller, J.L., Satterthwaite, A., Garrett-Sinha, L.A., Brombacher, F., and Zikherman, J. (2018). IgM and IgD B cell receptors differentially respond to endogenous antigens and control B cell fate. Elife *7*, e35074. https://doi.org/10.7554/eLife.35074.
12. Naito, Y., Takematsu, H., Koyama, S., Miyake, S., Yamamoto, H., Fujinawa, R., Sugai, M., Okuno, Y., Tsujimoto, G., Yamaji, T., et al. (2007). Germinal center marker GL7 probes activation-dependent repression of N-glycolylneuraminic acid, a sialic acid species involved in the negative modulation of B-cell activation. Mol. Cell Biol. *27*, 3008–3022. https://doi.org/10.1128/MCB.02047-06.
13. Zawil, L., Marchiol, T., Brauge, B., Saintamand, A., Carrion, C., Dessauge, E., Oblet, C., Le Noir, S., Mourcin, F., Brousse, M., et al. (2022). Distinct B-Cell Specific Transcriptional Contexts of the BCL2 Oncogene Impact Pre-Malignant Development in Mouse Models. Cancers *14*, 5337. https://doi.org/10.3390/cancers14215337.
14. Haas, K.M. (2015). B-1 lymphocytes in mice and nonhuman primates. Ann. N. Y. Acad. Sci. *1362*, 98–109. https://doi.org/10.1111/nyas.12760.
15. Ma, S., Caligiuri, M.A., and Yu, J. (2022). A four-stage model for murine natural killer cell development in vivo. J. Hematol. Oncol. *15*, 31. https://doi.org/10.1186/s13045-022-01243-1.
16. Hu, Z., Gu, W., Wei, Y., Liu, G., Wu, S., and Liu, T. (2019). NKT Cells in Mice Originate from Cytoplasmic CD3-Positive, CD4(-)CD8(-) Double-Negative Thymocytes that Express CD44 and IL-7Ralpha. Sci. Rep. *9*, 1874. https://doi.org/10.1038/s41598-018-37811-0.
17. Jiang, Y., Li, Y., and Zhu, B. (2015). T-cell exhaustion in the tumor microenvironment. Cell Death Dis. *6*, e1792. https://doi.org/10.1038/cddis.2015.162.
18. Gerberick, G.F., Cruse, L.W., Miller, C.M., Sikorski, E.E., and Ridder, G.M. (1997). Selective modulation of T cell memory markers CD62L and CD44 on murine draining lymph node cells following allergen and irritant treatment. Toxicol. Appl. Pharmacol. *146*, 1–10. https://doi.org/10.1006/taap.1997.8218.
19. Kassiotis, G., Gray, D., Kiafard, Z., Zwirner, J., and Stockinger, B. (2006). Functional specialization of memory Th cells revealed by expression of integrin CD49b. J. Immunol. *177*, 968–975. https://doi.org/10.4049/jimmunol.177.2.968.
20. Murray, T., Fuertes Marraco, S.A., Baumgaertner, P., Bordry, N., Cagnon, L., Donda, A., Romero, P., Verdeil, G., and Speiser, D.E. (2016). Very Late Antigen-1 Marks

Functional Tumor-Resident CD8 T Cells and Correlates with Survival of Melanoma Patients. Front. Immunol. *7*, 573. https://doi.org/10.3389/fimmu.2016.00573.

21. Chevrier, S., Genton, C., Kallies, A., Karnowski, A., Otten, L.A., Malissen, B., Malissen, M., Botto, M., Corcoran, L.M., Nutt, S.L., and Acha-Orbea, H. (2009). CD93 is required for maintenance of antibody secretion and persistence of plasma cells in the bone marrow niche. Proc. Natl. Acad. Sci. USA *106*, 3895–3900. https://doi.org/10.1073/pnas.0809736106.

22. Daley, J.M., Thomay, A.A., Connolly, M.D., Reichner, J.S., and Albina, J.E. (2008). Use of Ly6G-specific monoclonal antibody to deplete neutrophils in mice. J. Leukoc. Biol. *83*, 64–70. https://doi.org/10.1189/jlb.0407247.

23. Youn, J.I., Nagaraj, S., Collazo, M., and Gabrilovich, D.I. (2008). Subsets of myeloid-derived suppressor cells in tumor-bearing mice. J. Immunol. *181*, 5791–5802. https://doi.org/10.4049/jimmunol.181.8.5791.

24. Aizawa, H., Zimmermann, N., Carrigan, P.E., Lee, J.J., Rothenberg, M.E., and Bochner, B.S. (2003). Molecular analysis of human Siglec-8 orthologs relevant to mouse eosinophils: identification of mouse orthologs of Siglec-5 (mSiglec-F) and Siglec-10 (mSiglec-G). Genomics *82*, 521–530. https://doi.org/10.1016/s0888-7543(03)00171-x.

25. Merad, M., Sathe, P., Helft, J., Miller, J., and Mortha, A. (2013). The dendritic cell lineage: ontogeny and function of dendritic cells and their subsets in the steady state and the inflamed setting. Annu. Rev. Immunol. *31*, 563–604. https://doi.org/10.1146/annurev-immunol-020711-074950.

26. Dos Anjos Cassado, A. (2017). F4/80 as a Major Macrophage Marker: The Case of the Peritoneum and Spleen. Results Probl. Cell Differ. *62*, 161–179. https://doi.org/10.1007/978-3-319-54090-0_7.

27. Terrazas, C., Varikuti, S., Oghumu, S., Steinkamp, H.M., Ardic, N., Kimble, J., Nakhasi, H., and Satoskar, A.R. (2017). Ly6C(hi) inflammatory monocytes promote susceptibility to Leishmania donovani infection. Sci. Rep. *7*, 14693. https://doi.org/10.1038/s41598-017-14935-3.

28. Imhof, B.A., Jemelin, S., Ballet, R., Vesin, C., Schapira, M., Karaca, M., and Emre, Y. (2016). CCN1/CYR61-mediated meticulous patrolling by Ly6Clow monocytes fuels vascular inflammation. Proc. Natl. Acad. Sci. USA *113*, E4847–E4856. https://doi.org/10.1073/pnas.1607710113.

29. VanGundy, Z.C., Guerau-de-Arellano, M., Baker, J.D., Strange, H.R., Olivo-Marston, S., Muth, D.C., and Papenfuss, T.L. (2014). Continuous retinoic acid induces the differentiation of mature regulatory monocytes but fails to induce regulatory dendritic cells. BMC Immunol. *15*, 8. https://doi.org/10.1186/1471-2172-15-8.

30. Hengesbach, L.M., and Hoag, K.A. (2004). Physiological concentrations of retinoic acid favor myeloid dendritic cell development over granulocyte development in cultures of bone marrow cells from mice. J. Nutr. *134*, 2653–2659. https://doi.org/10.1093/jn/134.10.2653.

31. Kusuka, Y., Kajiwara, C., Shimada, S., Ishii, Y., Miyazaki, Y., Inase, N., Standiford, T.J., and Tateda, K. (2018). Potential Role of Gr-1+ CD8+ T Lymphocytes as a Source of Interferon-γ and M1/M2 Polarization during the Acute Phase of Murine *Legionella pneumophila Pneumonia*. J. Innate Immun. *10*, 328–338. https://doi.org/10.1159/000490585.

32. Zhu, J., Feng, B., Xu, Y., Chen, W., Sheng, X., Feng, X., Shi, X., Liu, J., Pan, Q., Yu, J., et al. (2020). Mesenchymal stem cells alleviate LPS-induced acute lung injury by inhibiting the proinflammatory function of Ly6C(+) CD8(+) T cells. Cell Death Dis. *11*, 829. https://doi.org/10.1038/s41419-020-03036-1.

33. Cervenak, L., Magyar, A., Boja, R., and László, G. (2001). Differential expression of GL7 activation antigen on bone marrow B cell subpopulations and peripheral B cells. Immunol. Lett. *78*, 89–96. https://doi.org/10.1016/s0165-2478(01)00239-5.

34. Laszlo, G., Hathcock, K.S., Dickler, H.B., and Hodes, R.J. (1993). Characterization of a novel cell-surface molecule expressed on subpopulations of activated T and B cells. J. Immunol. *150*, 5252–5262.

35. Kim, Y., Saini, U., Kim, D., Hernandez-Aguirre, I., Hedberg, J., Martin, A., Mo, X., Cripe, T.P., Markert, J., Cassady, K.A., and Dhital, R. (2024). Enhanced IL-12 transgene expression improves oncolytic viroimmunotherapy. Front. Immunol. *15*, 1375413. https://doi.org/10.3389/fimmu.2024.1375413.

36. Ma, R., Lu, T., Li, Z., Teng, K.Y., Mansour, A.G., Yu, M., Tian, L., Xu, B., Ma, S., Zhang, J., et al. (2021). An Oncolytic Virus Expressing IL15/IL15Rα Combined with Off-the-Shelf EGFR-CAR NK Cells Targets Glioblastoma. Cancer Res. *81*, 3635–3648. https://doi.org/10.1158/0008-5472.Can-21-0035.

37. Currier, M.A., Sprague, L., Rizvi, T.A., Nartker, B., Chen, C.Y., Wang, P.Y., Hutzen, B.J., Franczek, M.R., Patel, A.V., Chaney, K.E., et al. (2017). Aurora A kinase inhibition enhances oncolytic herpes virotherapy through cytotoxic synergy and innate cellular immune modulation. Oncotarget *8*, 17412–17427. https://doi.org/10.18632/oncotarget.14885.

38. Xu, B., Ma, R., Russell, L., Yoo, J.Y., Han, J., Cui, H., Yi, P., Zhang, J., Nakashima, H., Dai, H., et al. (2018). An oncolytic herpesvirus expressing E-cadherin improves survival in mouse models of glioblastoma. Nat. Biotechnol. *37*, 45–94. https://doi.org/10.1038/nbt.4302.

39. Hänninen, A., Maksimow, M., Alam, C., Morgan, D.J., and Jalkanen, S. (2011). Ly6C supports preferential homing of central memory CD8+ T cells into lymph nodes. Eur. J. Immunol. *41*, 634–644. https://doi.org/10.1002/eji.201040760.

40. Lancki, D.W., Hsieh, C.S., and Fitch, F.W. (1991). Mechanisms of lysis by cytotoxic T lymphocyte clones. Lytic activity and gene expression in cloned antigen-specific CD4+ and CD8+ T lymphocytes. J. Immunol. *146*, 3242–3249.

41. Ebnet, K., Chluba-de Tapia, J., Hurtenbach, U., Kramer, M.D., and Simon, M.M. (1991). In vivo primed mouse T cells selectively express T cell-specific serine proteinase-1 and the proteinase-like molecules granzyme B and C. Int. Immunol. *3*, 9–19. https://doi.org/10.1093/intimm/3.1.9.

42. Cachot, A., Bilous, M., Liu, Y.C., Li, X., Saillard, M., Cenerenti, M., Rockinger, G.A., Wyss, T., Guillaume, P., Schmidt, J., et al. (2021). Tumor-specific cytolytic CD4 T cells mediate immunity against human cancer. Sci. Adv. *7*, eabe3348. https://doi.org/10.1126/sciadv.abe3348.

43. Du, W., Leigh, N.D., Bian, G., Alqassim, E., O'Neill, R.E., Mei, L., Qiu, J., Liu, H., McCarthy, P.L., and Cao, X. (2016). Granzyme B Contributes to the Optimal Graft-Versus-Tumor Effect Mediated by Conventional CD4(+) T Cells. J. Immunol. Res. Ther. *1*, 22–28.

44. Dorothee, G., Vergnon, I., Menez, J., Echchakir, H., Grunenwald, D., Kubin, M., Chouaib, S., and Mami-Chouaib, F. (2002). Tumor-infiltrating CD4+ T lymphocytes express APO2 ligand (APO2L)/TRAIL upon specific stimulation with autologous lung carcinoma cells: role of IFN-alpha on APO2L/TRAIL expression and -mediated cytotoxicity. J. Immunol. *169*, 809–817. https://doi.org/10.4049/jimmunol.169.2.809.

45. Gondek, D.C., Lu, L.F., Quezada, S.A., Sakaguchi, S., and Noelle, R.J. (2005). Cutting edge: contact-mediated suppression by CD4+CD25+ regulatory cells involves a granzyme B-dependent, perforin-independent mechanism. J. Immunol. *174*, 1783–1786. https://doi.org/10.4049/jimmunol.174.4.1783.

46. Cao, X., Cai, S.F., Fehniger, T.A., Song, J., Collins, L.I., Piwnica-Worms, D.R., and Ley, T.J. (2007). Granzyme B and perforin are important for regulatory T cell-mediated suppression of tumor clearance. Immunity *27*, 635–646. https://doi.org/10.1016/j.immuni.2007.08.014.

47. Merkenschlager, J., Finkin, S., Ramos, V., Kraft, J., Cipolla, M., Nowosad, C.R., Hartweger, H., Zhang, W., Olinares, P.D.B., Gazumyan, A., et al. (2021). Dynamic regulation of T(FH) selection during the germinal centre reaction. Nature *591*, 458–463. https://doi.org/10.1038/s41586-021-03187-x.

48. De Silva, N.S., and Klein, U. (2015). Dynamics of B cells in germinal centres. Nat. Rev. Immunol. *15*, 137–148. https://doi.org/10.1038/nri3804.

49. Spear, S., Candido, J.B., McDermott, J.R., Ghirelli, C., Maniati, E., Beers, S.A., Balkwill, F.R., Kocher, H.M., and Capasso, M. (2019). Discrepancies in the Tumor Microenvironment of Spontaneous and Orthotopic Murine Models of Pancreatic Cancer Uncover a New Immunostimulatory Phenotype for B Cells. Front. Immunol. *10*, 542. https://doi.org/10.3389/fimmu.2019.00542.

50. Cui, C., Wang, J., Fagerberg, E., Chen, P.M., Connolly, K.A., Damo, M., Cheung, J.F., Mao, T., Askari, A.S., Chen, S., et al. (2021). Neoantigen-driven B cell and CD4 T follicular helper cell collaboration promotes anti-tumor CD8 T cell responses. Cell *184*, 6101–6118.e13. https://doi.org/10.1016/j.cell.2021.11.007.

51. Sautès-Fridman, C., Petitprez, F., Calderaro, J., and Fridman, W.H. (2019). Tertiary lymphoid structures in the era of cancer immunotherapy. Nat. Rev. Cancer *19*, 307–325. https://doi.org/10.1038/s41568-019-0144-6.

52. Nguyen, A.A., and Platt, C.D. (2024). Flow Cytometry-based Immune Phenotyping of T and B Lymphocytes in the Evaluation of Immunodeficiency and Immune Dysregulation. Clin. Lab. Med. *44*, 479–493. https://doi.org/10.1016/j.cll.2024.04.009.

53. Donadeu, L., Jouve, T., Bin, S., Hartzell, S., Crespo, E., Torija, A., Jarque, M., Kervella, D., Zúñiga, J., Zhang, W., et al. (2024). High-dimensional mass cytometry identified circulating natural killer T-cell subsets associated with protection from cytomegalovirus infection in kidney transplant recipients. Kidney Int. *106*, 482–495. https://doi.org/10.1016/j.kint.2024.03.027.

54. Cassady, K.A. (2005). Human cytomegalovirus TRS1 and IRS1 gene products block the double-stranded-RNA-activated host protein shutoff response induced by herpes simplex virus type 1 infection. J. Virol. *79*, 8707–8715. https://doi.org/10.1128/JVI.79.14.8707-8715.2005.

55. Parasuraman, S., Raveendran, R., and Kesavan, R. (2010). Blood sample collection in small laboratory animals. J. Pharmacol. Pharmacother. *1*, 87–93. https://doi.org/10.4103/0976-500X.72350.

56. Soleimani, M., and Nadri, S. (2009). A protocol for isolation and culture of mesenchymal stem cells from mouse bone marrow. Nat. Protoc. *4*, 102–106. https://doi.org/10.1038/nprot.2008.221.